Sulfate Attack on Cement Paste with Volcanic Ash: Durability Analysis

by
Maranda Lee Johnston

Submitted to the
Department of Materials Science and Engineering
in Partial Fulfillment of the Requirements for the Degree of

Bachelor of Science

at the

Massachusetts Institute of Technology

June 2017

Signature of Author: Signature redacted
Department of Materials Science and Engineering
12/10/2016 Date

Certified By: Signature redacted
Oral Buyukozturk
Professor of Civil and Environmental Engineering
Thesis Advisor

Read By: Signature redacted
Elsa Olivetti
Assistant Professor of Materials Science and Engineering
Thesis Reader

Accepted by: Signature redacted
Geoffrey S.D. Beach
Professor of Materials Science and Engineering
Chair, Department Undergraduate Committee

Table of Contents

Abstract

Sulfate attack is responsible for deterioration of infrastructure and often occurs in sulfate rich soil or brackish environment. The aim of this study is to investigate the effect of volcanic ash cements when exposed to different forms of sulfate attack, specifically to sodium and magnesium sulfates. Pozzolanic volcanic ash can be a viable partial substitute for Portland Cements to develop cement paste compositions for superior sulfate resistance with potential for durability and sustainable solutions. Pumiceous volcanic ash was used in preparing Roman hydraulic pozzolan concrete that was used to build the Bay of Naples. This study reports the microstructural and mechanical characterization of cement paste with volcanic ash when exposed to accelerated sulfate attack via electrokinetics. The test specimens were exposed to sodium and magnesium sulfate solutions for a period of 30 days. The effect of gradual decomposition of calcium-silicate-hydrate (C-S-H) gel was examined using Raman spectroscopy and Magic Angle Nuclear Magnetic Resonance (MAS NMR), while the mechanical properties were determined using nanoindentation and compression tests. Exposure to magnesium sulfate solution led to formation of magnesium-silicate-hydrate (M-S-H) along with crystallization of gypsum and brucite, while exposure to sodium sulfates led to the formation of thenardite and mirabilite. An optimum mix combination of 10-30% partial substitution of volcanic ash was determined for optimal sulfate resistance and compressive strength. This mix combination was determined by considering the resulting mechanical, micro and pore structure characteristics of the hardened cement pastes.

Acknowledgements

I would like to thank Dr. Kunal Kupwade-Patil, Professor Oral Buyukozturk, without whom this thesis would not be possible. Their continued support, expertise, and resources were essential to this project, and to that I am truly thankful.

I would also like to thank Professor Elsa Olivetti, and Professor John Ochsendorf for their support throughout this project. I would like to thank Dr. Alan Schwartzman for his help with the nanoindentation, and Vern Robertson and Shibata Masateru of JEOL for their help with the SEM. Use of the Advanced Photon Source at Argonne National Laboratory was supported by the U.S. Department of Energy, Office of Department of Energy, Office of Science, Office of Basic Energy Sciences, under Contract No. DE-AC02- 06CH11357. I would like to thank 11-BM staff Dr. Saul H. Lapidus and Lynn Ribaud.

This project was partially sponsored by the "Kuwait Foundation for the Advancement of Sciences." This research was conducted in the context of the Kuwait-MIT signature project on sustainability of built environment, under the direction of Professor Oral Buyukozturk.

I would also like to thank my parents, Caroline and Chuck Johnston, Sean Lowder, Libby Koolik, Allison Edwards, Caroline Walsh, Courtney Diamond, and many others for their support throughout my undergraduate career.

List of Figures

List of Tables

1. Introduction and Motivation

1.1 A brief history of cement

Concrete is one of the most abundantly used materials in the world, dating back thousands of years. The Romans revolutionized the use of concrete during the period of Praeneste's construction, as they made pozzolana from the volcanic ash from the Vesuvius area [1]. Pozzolana is a siliceous material (sometimes with aluminum) that reacts with calcium hydroxide in the presence of water at room temperature, creating a product with cementitious properties. This cement paste can be combined with fine aggregate, such as sand, to create mortar and finally, the mortar can be combined with larger aggregate to make concrete. The most noted use of concrete in Roman architecture is the dome of the Pantheon. The dome is completed made of small batches of concrete that were immediately poured into a temporary wooden formwork [1]. Modern concrete is the same in principle, cement, mortar, and large aggregates are mixed to create concrete. The most common type of cement utilized today is Ordinary Portland Cement, which is named for its similarity to Portland stone, a building stone [2]. Portland cement consists primarily of lime, silica, and alumina. In the presence of water, these ingredients react to form hydrated calcium silicates, that form a hydrated product. Cement can be mixed with aggregates to create concrete through a series of chemical reactions. Although the idea is the same, today's concrete has the issue of sulfate attack, which did not plague the Roman cement. Today, sulfate attack is a concern for building foundations as well as other structures.

1.2 A look into sulfate attack

Sulfate attack on concrete has been reported from many parts of the world. From as early as 1936, the concrete construction manual published by the U.S. Bureau of Reclamation warned that concentrations of soluble sulfates greater than 0.1% in soil may have a deleterious effect on

concrete, and more than 0.5% soluble sulfate in soil may have a serious effect. While sulfate is acknowledged to have an effect on the concrete, the mechanisms of sulfate attack are not completely understood. This study aims to analyze the microstructural and mechanical properties of cement paste samples subjected to accelerated sulfate attack via electrokinetic treatment.

Sodium sulfate reacts with the cement to form sodium hydroxide, which ensures the continuation of the high alkalinity in the system, which is essential for the stability of the cementitious material, specifically for the stability of the calcium-silicate-hydrate (C-S-H) hydration product (See Equation 1). On the other hand, magnesium sulfate reacts with the cement to form magnesium based hydration products (See Equations 2 and 3). With the magnesium sulfate reaction, calcium hydroxide is converted to gypsum, which is accompanied by the simultaneous formation of magnesium hydroxide, which is relatively insoluble. In the absence of hydroxyl ions in the solution, C-S-H is no longer stable and is also attacked by the sulfate solution. The magnesium sulfate attack should, therefore, be more severe on concrete than sodium sulfate attack.

$$Na_2SO_4 + Ca(OH)_2 + 2H2O \rightarrow CaSO_4 \cdot 2H_2O + 2NaOH \quad (1)$$

$$MgSO_4 + Ca(OH)_2 + 2H_2O \rightarrow CaSO_4 \cdot 2H_2O + Mg(OH)_2 \quad (2)$$

$$3MgSO_4 + 3CaO \cdot 2SiO_2 \cdot 3H_2O + 8H_2O \rightarrow 3CaSO4 \cdot 2H2O + 3Mg(OH)_2 + 2SiO_2 \cdot H_2O \quad (3)$$

1.3 Using volcanic ash for environmental, economical, and strength advantages

Volcanic ash was chosen as a partial substitute for Portland cement for environmental, economical, and chemical reasons. This project was partially sponsored by the "Kuwait Foundation for the Advancement of Sciences," and as such, there was a focus on the status of cement and concrete usage in Kuwait. It is very expensive to make durable concretes in Kuwait, as raw materials need to be imported from Europe and North America. However, there is an abundance of volcanic rocks in the surrounding areas. These volcanic eruption by-products are

often trucked to landfills, which is expensive and harmful to the environment. Utilization of volcanic ash in concrete would cuts costs and could offer better mechanical properties for the concrete. Volcanic ash may also have a positive effect on sulfate attack, as volcanic ash contains a high alumnia content, which leads to the formation of a binding gel known as calcium-aluminio-silicate-hydrate (C-A-S-H) gel. The inclusion of volcanic ash can also lead to the formation of magnesium-silicate-hydrate (M-S-H) gel. M-S-H can be present in the crystalline, or amorphous phase. Crystalline M-S-H has a spherical structure, whereas C-S-H, a common cement hydration product, has a columnar structure [3]. In the amorphous phase, M-S-H may lead to the stability of C-S-H. These properties could lead to a high strength concrete, that may have increased sulfate resistance.

1.4 Objective and Approach

The objective of this study is to characterize the magnesium and sodium sulfate effect on samples prepared with volcanic ash and Ordinary Portland Cement. As the effect of sulfates is not entirely understood, a multi-scale approach will be taken to understand the mechanical as well as pore and microstructural properties of the cement paste samples. At the Angstrom scale, the Synchrotron X-ray Diffraction can help to determine which phases are present in the sample. ^{29}Si Magic Angle Spinning Nuclear Magnetic Resonance (^{29}Si MAS NMR) is on the molecular scale, and gives information about the connectivity of the silica tetrahedron present in the cement paste samples. This can be used to determine which hydration products are present. While the nano-scale gives information about the individual phase pore and microstructure, the bulk compressive testing can give information about the cement paste on the macroscale.

2. Materials and Methods

2.1 Materials

Cement paste was made from Ordinary Portland Cement (OPC) from Kuwait Cement Company and volcanic ash procured from the Kingdom of Saudi Arabia. OPC and volcanic ash were measured using a laser based particle size analyzer. The volcanic ash was ground to a finer size using a high speed vibratory ball mill to a mean particle size of 17 μm, which was chosen as a result of previous study (currently in submission). Type V cement paste from Lehigh Hanson was also analyzed as a baseline. Type V cement is characterized as high sulfate resistant cement, however, the exact composition of the cement used is proprietary knowledge.

After curing, the samples were subjected to .352 molarity sodium sulfate and .352 molarity magnesium sulfate as per ASTM C1012.

2.2 Mixing

Initial dry mixing of the volcanic ash and OPC was performed using a Daigger vortex-genie 2 mixer at 3200 rpm. Mixing was performed to ensure that the volcanic ash was uniformly mixed with the OPC before exposing to de-ionized water. Samples were given a nomenclature that identified the percentage replacement of volcanic ash, with IP denoting the volcanic ash content. For example, 30wt% volcanic ash is denoted as IP-30. The specimens were cured for 28 days after mixing, and to retard the hydration, the samples were inserted in acetone immediately after curing.

Table 1. Composition of Volcanic Ash and Ordinary Portland Cement

OPC (%)	IP (%)	Type V (%)	Nomenclature
100	00	00	OPC
90	10	00	IP-10
70	30	00	IP-30
50	50	00	IP-50
0	0	100	Type V

OPC: Ordinary Portland Cement,

IP: Volcanic ash with a mean size of 17μm

2.3 Accelerated Sulfate Attack treatments

The samples were subjected to the .352 M Na_2SO_4 and $MgSO_4$ per ASTM C1012 using the method developed by Cardeneas, *et al.* A container with a solution-to-specimen immersion of 4:1 at 23°C for 30 days was utilized. The circuit can be seen in Figure 1 below. The applied current density was 1 A/m^2 as calculated over the outside surface area of the cylinder, and the solution was replaced weekly [4].

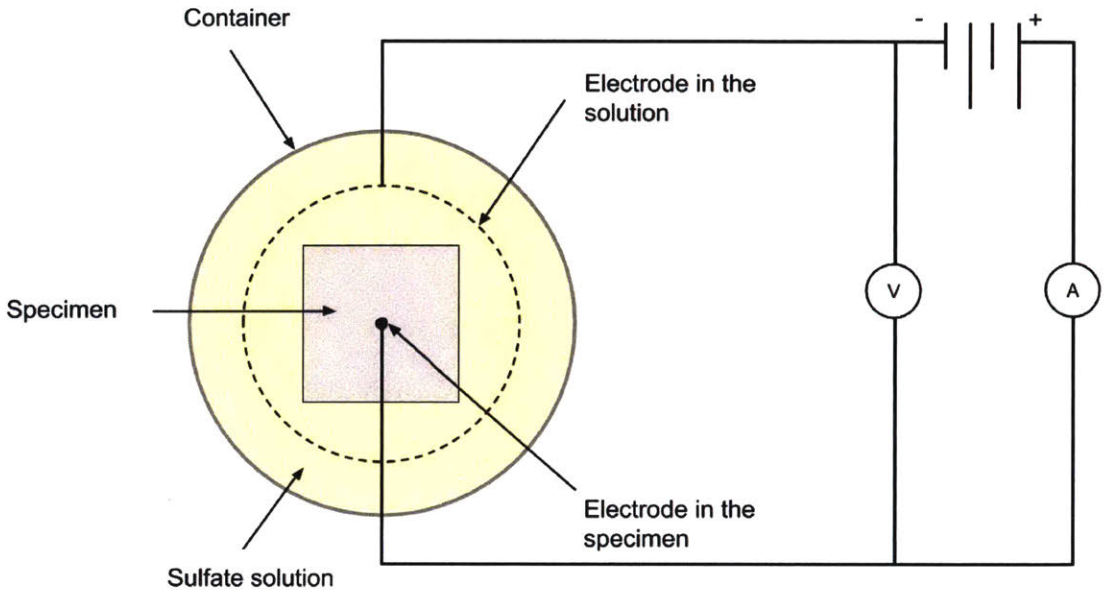

Fig. 1 Circuit Diagram of sulfate exposure

2.4 Methods

Elastic properties of the cement pastes were analyzed via bulk compression testing and nanoindentation testing. Q quantification was performed with ^{29}Si MAS NMR. Synchrotron XRD was completed at the Argonne National Lab. Scanning Electron Microscopy was completed at JEOL in Peabody, MA. All characterization techniques can be seen in Table 2.

Table 2. Characterization Techniques Utilized for Cement Paste Samples

Characterization Technique	**Sample Type**	**Measures**
Mechanical Analysis		
Compression Test	Solid	Strength
Nanoindentation	Solid (polished)	Elastic modulus
Microstructure		
Scanning Electron Microscopy	Solid	Morphology
^{29}Si MAS NMR	Powder	Phases and Bonding
Synchrotron XRD	Powder	Phases
Nanoindentation	Solid (polished)	Phases

2.4.1 Compression Test Analysis

Compression testing was utilized to determine the bulk compressive strength of the sample. The compression testing was completed to ASTM C109 [5]. In accordance with this standard, cement paste samples were cured in 50-mm cubes and subjected to testing. The rate used for testing was 20 MPa/min, as the standard recommends a rate between 900-1800 N/s. The samples were loaded to failure, and the compressive strength was determined by dividing the maximum load by the cross-sectional area of the sample.

2.4.2 Nanoindentation

Nanoindentation was performed to determine the Young's modulus and hardness of micron sized areas of the sample. This technique was utilized to help determine which phases contributed to the bulk compressive strength. In preparation for the nanoindentation, samples were sent to Wagner Petrographic in Lindon, UT to be set in epoxy and polished to a surface roughness of approximately 50 nm. When the samples were returned to MIT, they were indented by the author the MIT Nanolab with the Hysitron TriboIndenter nanoindenter. Each sample was indented in a 9 x 9 grid, with the rows and columns spaced 5μm apart, for a total of 81 indents for each sample.

Each indent was loaded to 2mN in a 10 second span, held at 2mN for 5 seconds, and unloaded for 10 seconds. A fused quartz sample was used as a reference for the area function. The Hysitron TriboIndenter outputs the reduced modulus (E_r) and the sample hardness. Using Equation 4, the sample Young's Modulus can be calculated [6].

$$\frac{1}{E_r} = \frac{(1-\nu_i^2)}{E_i} + \frac{(1-\nu_s^2)}{E_s} \tag{4}$$

2.4.3 ^{29}Si MAS NMR

^{29}Si Magic Angle Spinning Nuclear Magnetic Resonance (MAS NMR) was utilized for the chemical connectivity of the silica tetrahedron. This information can help determine the Al/Si ratio, which can be linked to C-S-H and C-A-S-H content. The ^{29}Si MAS NMR was chosen as it has a low sensitivity nucleus which has spin ½ and yields sharp lines. Silicon has a wide chemical shift so it is good for determining the chemical environment in silicon compounds. ^{29}Si MAS NMR provides quantitative information on the fractions of silicon present in different tetrahedral environments.

The samples were sent to Kuwait University for ^{29}Si Magic Angle Spinning Nuclear Magnetic Resonance (MAS NMR). The ^{29}Si MAS NMR produces spectra of the sample which can be deconvoluted and assigned to specific q-quantification values. The deconvoluted spectra was sent to the author, and she assigned Q^n values to the curves. Q^n denotes the connectivity of the silicate tetrahedron, ranging from 0 to 4. With this in mind, Q^0 represents isolated tetrahedral, Q^1 denotes chain end group tetrahedral, Q^2 denotes middle groups, Q^3 denotes branching site, and Q^4 denotes cross-linking sites in three-dimensional framework [7]. From this information, the alumina to silica ratio can be calculated using Equation 5 [8].

$$\frac{Al}{Si} = \frac{0.5\,Q^2(1Al)}{Q^1 + Q_p^2 + Q_b^2 + Q^2(1Al)} \quad (5)$$

2.4.4 Synchrotron XRD

Synchrotronic XRD was performed to assess the cementitious phases present in the sample. The testing was completed using the powder diffractometer on 11BM at the Advance Photon Source, Argonne National Lab, Lemont, IL. The sample was ground into a fine powder (grain size = 1-10 mm) and then sent to Argonne National Lab within Linderman tubes (F = 0.3 mm). The 11BM utilized a monochromatic beam which is extracted from the white beam by means of a double Si(111) monochrometer. The sample is rotated along the capillary axis to reduced preferred orientation problems inherent to layered compounds. The wavelength of the X-ray was 0.4142 Å, with a fixed energy of 30 keV, and data was recorded with a 2θ range from 1 to 45 with a counting time of 1 hour. The raw data was sent to the author which was then analyzed using High Score Plus from the Center of Materials Science of MIT.

2.4.5 Scanning Electron Microscopy Analysis

SEM was utilized to observe the surface microstructure, which can give an indication of the phases present in the samples. The cement paste samples were taken to the JEOL facility in Peabody, MA for scanning electron microscopy using the JEOL 2100F SEM. The author worked with a team of experts to observe the surface of the samples between 1.5-5kV.

3. Results and Discussion

3.1 Compression test analysis

Compression strength provides the bulk strength of the specimen. Figure 2 illustrates the bulk compressive testing results in the form of compressive strength. Looking specifically at Type V and IP10, these have higher strengths than the other samples, which suggests the sodium sulfate

reacted with the additional calcium, alumina, and silica from the fly ash in Type V, and the volcanic ash in IP10. These reactions form C-S-H, along with C-A-S-H related phases.

On the other hand, IP30 and IP50 sodium sulfate have less strength, which may be due to the increased volcanic ash content, which directly leads to an increase in magnesium, which is associated with the M-S-H phase. The M-S-H phase is responsible for deterioration of strength due to the incompatibility of the spherical M-S-H phase and the columnar C-S-H phase.

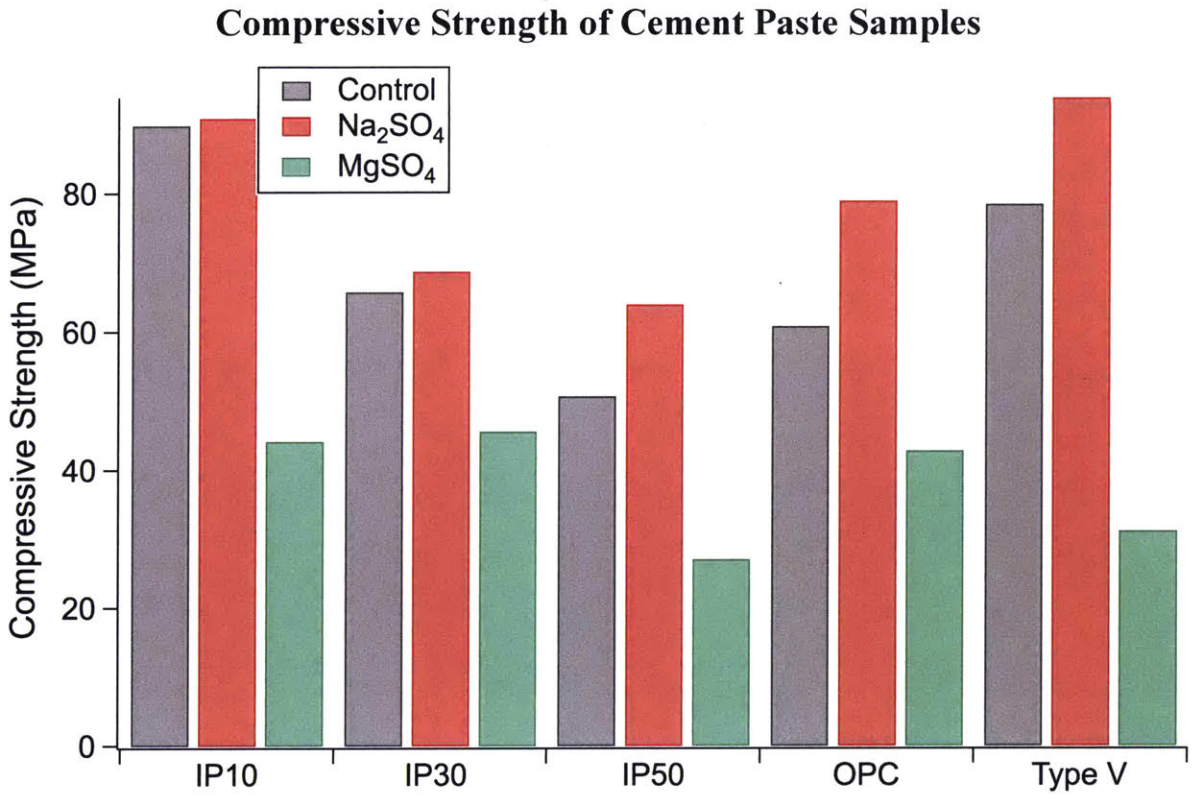

Fig. 2 Compression Strength Test for controls, Type V and OPC/VA combination

3.2 Nano-indentation

Nanoindentation generated curves of load vs depth, an example of which can be seen in Figure 3, which is an example of the average depth of displacement for IP30 Control, $MgSO_4$, and Na_2SO_4. These curves illustrate the load function setup: 10 seconds of loading, 5 seconds constant

at 2 micro-Newtons, and unloading for 10 seconds. The reduced modulus is calculated from the slope of the unloading curve.

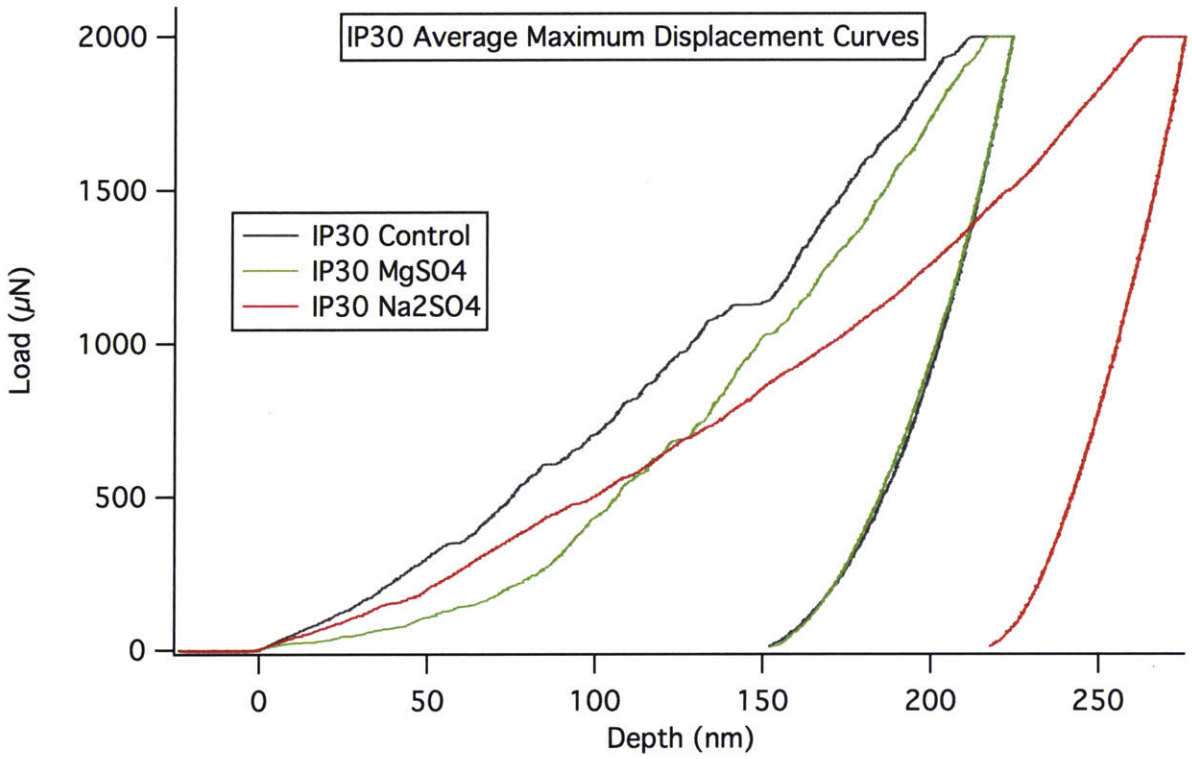

Fig. 3 Example of Nanoindentation Curve for IP30 Sample

Using Equation 4, the Young's Modulus can be calculated from the Reduced Modulus. The constants v_i and E_i are properties of the diamond tip indenter, are 0.07 and 1140 GPa, respectively [6]. The Poisson's ratio of the cement sample was chosen to be 0.24, as typical cement paste Poisson's ratio values are between 0.20 - 0.25 [9]. The calculated values are shown in Figure 4. The standard deviation of the samples, and therefore the error bars, was very large as the samples are heterogeneous and display a disparity in values. Figure 5 shows the maps of the reduced modulus and hardness of the samples, where each square represents an individual indent. These maps illustrate a sample size of 40x40 microns, and they illustrate the heterogeneity of the

samples. While most of the indents fall into the pink to purple range (around 20-50 GPa), some indents are in the green to yellow range, around 100 GPa. The variation in reduced modulus between indents may be due to the variation in particle size and chemistry of the volcanic ash. If the volcanic ash is properly engineered to a uniform particle size and chemistry, it may have better mechanical properties.

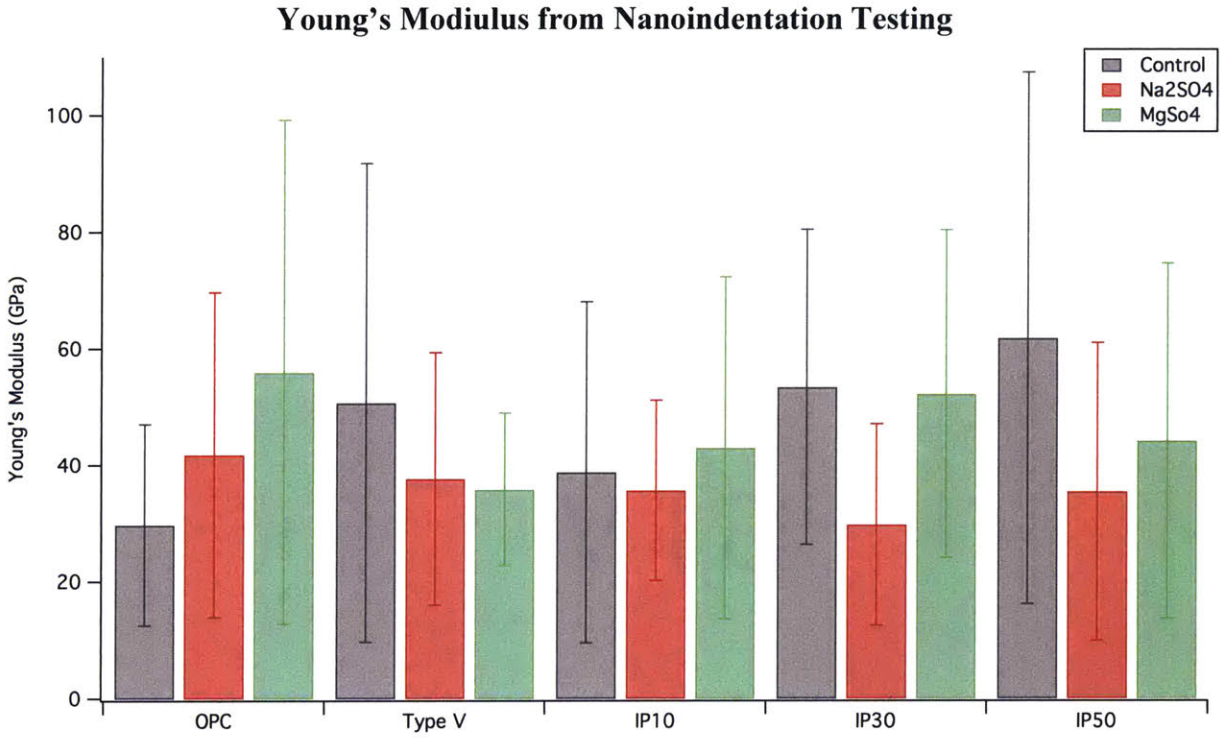

Fig. 4 Young's Modulus of nanoindentation samples

The reduced modulus of the samples may have direct contributions from C-S-H and C-A-S-H gels. The light pink color, around 18 ± GPa, may have contributions from low density C-S-H and the darker pink color, around 31 ± 4 GPa, may have contributions from high density C-S-H, according to the work of Jennings [10]. Based on the work of Puertas, the C-A-S-H region may be from 28-50 GPa, the light pink to the blue region [11]. The strength variation in these depends on the internal structure and cross-linking network of the C-A-S-H gels.

The IP30 sample has the maximum high density phases between 70-100 GPa. It may involve unreacted hydration products, which are much stronger than the reacted products. This is a technique that was utilized by the old Roman concrete, which had a majority of unreacted hydration products, which therefore helped in providing long lasting durability. This test, however, may not be representative of the whole sample, as it was only a 40x40 micron section of the sample.

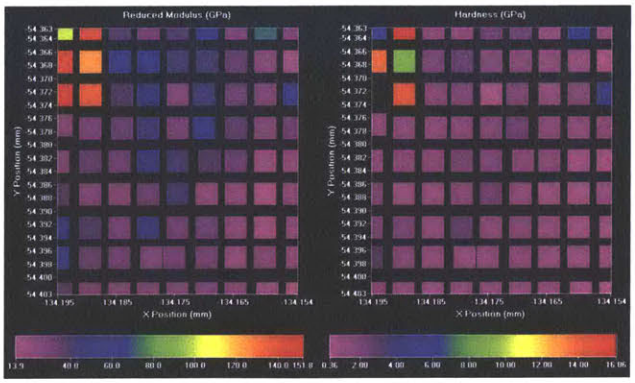

IP10 Control

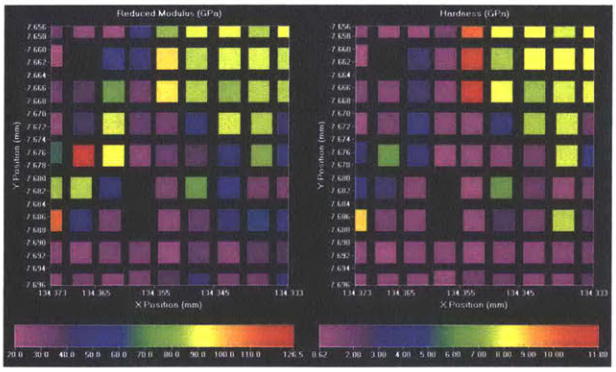

IP30 Control

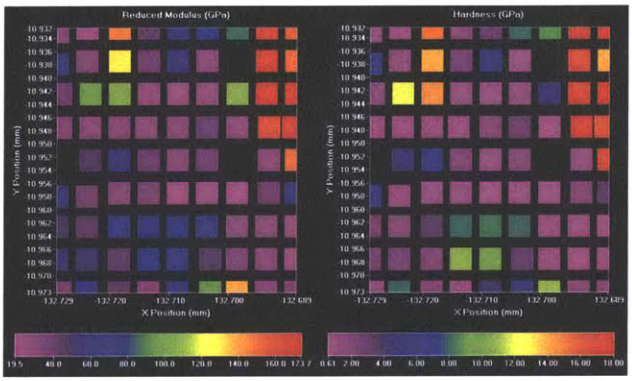

IP50 Control

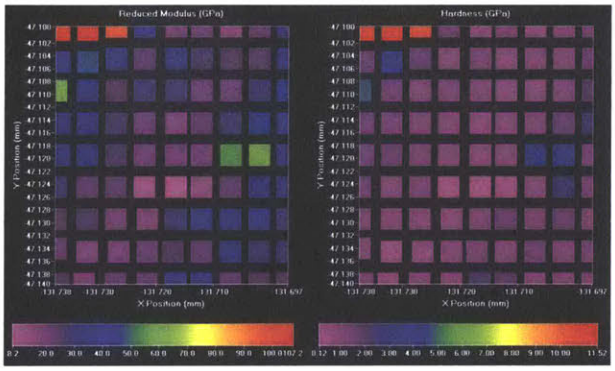

OPC Control

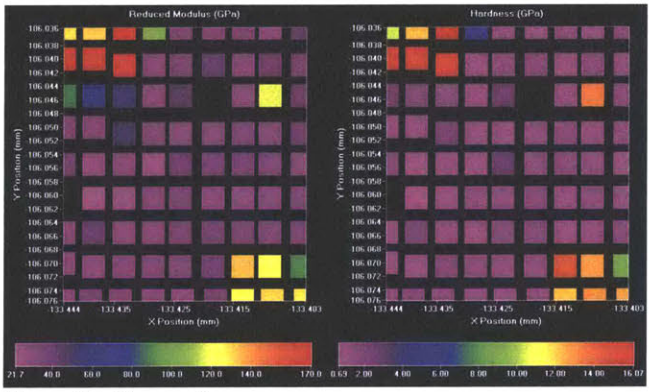

Type V Control

Fig. 5 Nanoindentation maps showing Reduced Modulus and Hardness from Control Samples

3.3 ^{29}Si MAS NMR Analysis

Figure 6 illustrates the deconvoluted spectrum given by the ^{29}Si MAS NMR for IP10 Control. From the deconvoluted peaks, the Q^n show the connectivity of the silicon tetrahedral. The other samples were analyzed in a similar manner. From the deconvoluted spectra, the chemical shift and area percentage can be assigned to Q^n values, by referencing literature values of Q^n values [12][13][14][15]. These can be illustrated in Tables 2-4. From these values, and using Equation 5, the Al/Si ratio can be calculated for the samples, which is shown in Figure 7.

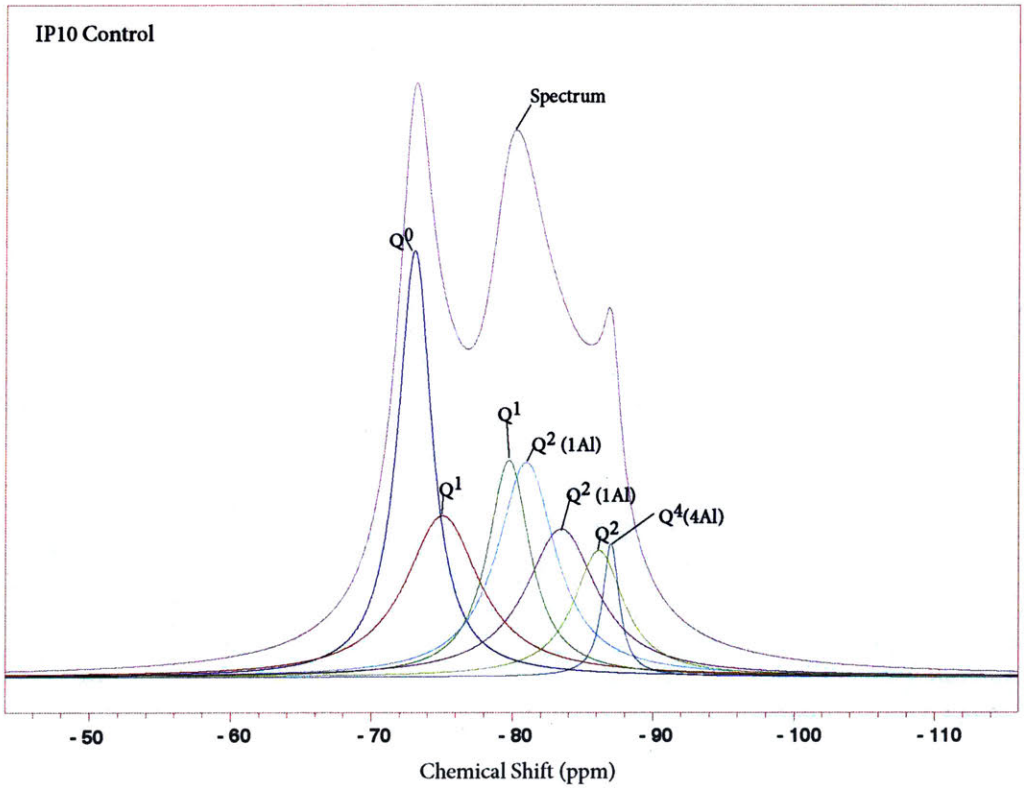

Fig. 6 Example of ^{29}Si MAS NMR Chemical Shift Deconvoluted Data

Table 3. Q^n assignments for control samples

Type V Control			**OPC Control**			**IP-50 Control**			**IP-30 Control**			**IP-10 Control**		
Assignment	Area (%)	Ppm	Assignment	Area (%)	Ppm	Assignment	Area (%)	Ppm	Assignment	Area (%)	Ppm	Assignment	Area (%)	ppm
Q^0		-74				Q^0	18	-73	Q^0	22	-74	Q^0	21	-73
Q^2 (1Al)		-82				Q^2 (1Al)	38	-82	Q^2 (1Al)	42	-81	Q^1	18	-75
Q^2		-86				Q^2 (1Al)	44	-83	Q^2 (0Al)	30	-85	Q^1	14	-80
Q^4 (nAl)		-93										Q^2 (1Al)	19	-81
												Q^2 (1Al)	16	-83
												Q^2	10	-86
												Q^4 (4Al)	3	-87

Table 4. Q^n assignments for $MgSO_4$ samples

Type V MgSO4			**OPC MgSO4**			**IP-50 MgSO4**			**IP-30 MgSO4**			**IP-10 MgSO4**		
Assignment	Area (%)	Ppm	Assignment	Area (%)	Ppm	Assignment	Area (%)	Ppm	Assignment	Area (%)	Ppm	Assignment	Area (%)	ppm
Q^0	24	-74	Q^0	24	-74	Q^0	12	-74	Q^0	17	-74	Q^0	26	-73
(1Al)	45	-81	(1Al)	46	-81	(1Al)	24	-81	(1Al)	34	-81	(1Al)	47	-81
(0Al)	31	-85	(0Al)	31	-85	(1Al)	25	-82	(0Al)	39	-84	(0Al)	27	-86
						(0Al)	39	-83	(0Al)	10	-86			

Table 5. Q^n assignments for Na_2SO_4 samples

Type V Na2SO4			OPC Na2SO4			IP-50 Na2SO4			IP-30 Na2SO4			IP-10 Na2SO4		
Assignment	Area (%)	Ppm	Assignment	Area (%)	Ppm	Assignment	Area (%)	Ppm	Assignment	Area (%)	Ppm	Assignment	Area (%)	ppm
			Q0	18	-73	Q1	17	-76	Q0	33	-74	Q0	25	-73
			Q1	30	-80	Q2	54	-84	Q2 (1Al)	67	-82	Q2 (1Al)	45	-81
			Q2 (1Al)	40	-81	Q4 (4Al)	29	-91				Q2 (0Al)	30	-85
			Q2	11	-86									

While it is acknowledged that there is ambiguity between the C-S-H and C-A-S-H gel phases, there is the possibility that the Al/Si ratio can help to identify the relative strength contributions of the gels. The Al/Si ratio has been graphed in Figure 7, and these values can be compared to the literature values shown in Figure 8. From these values, the controls may have more contributions from C-S-H than C-A-S-H. On the other hand, the sulfate samples seem to have higher contributions of C-A-S-H.

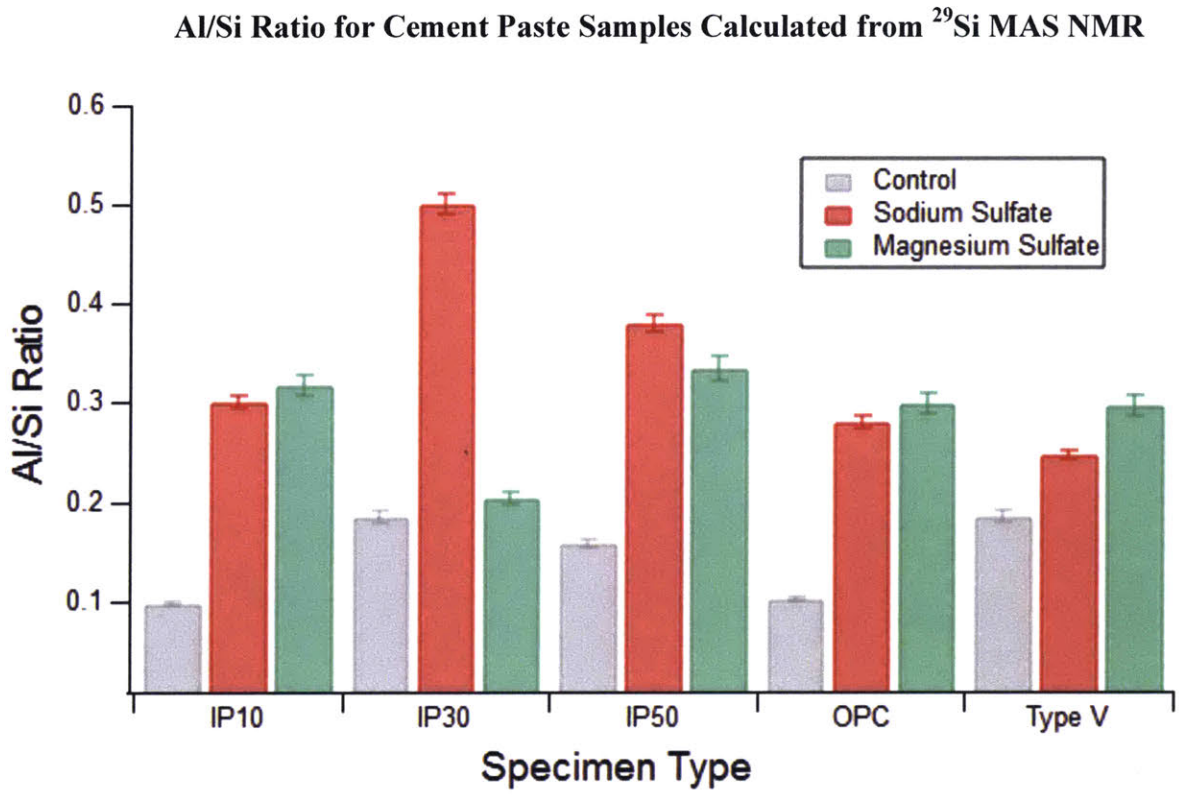

Fig. 7 Al/Si ratio for samples from NMR Data

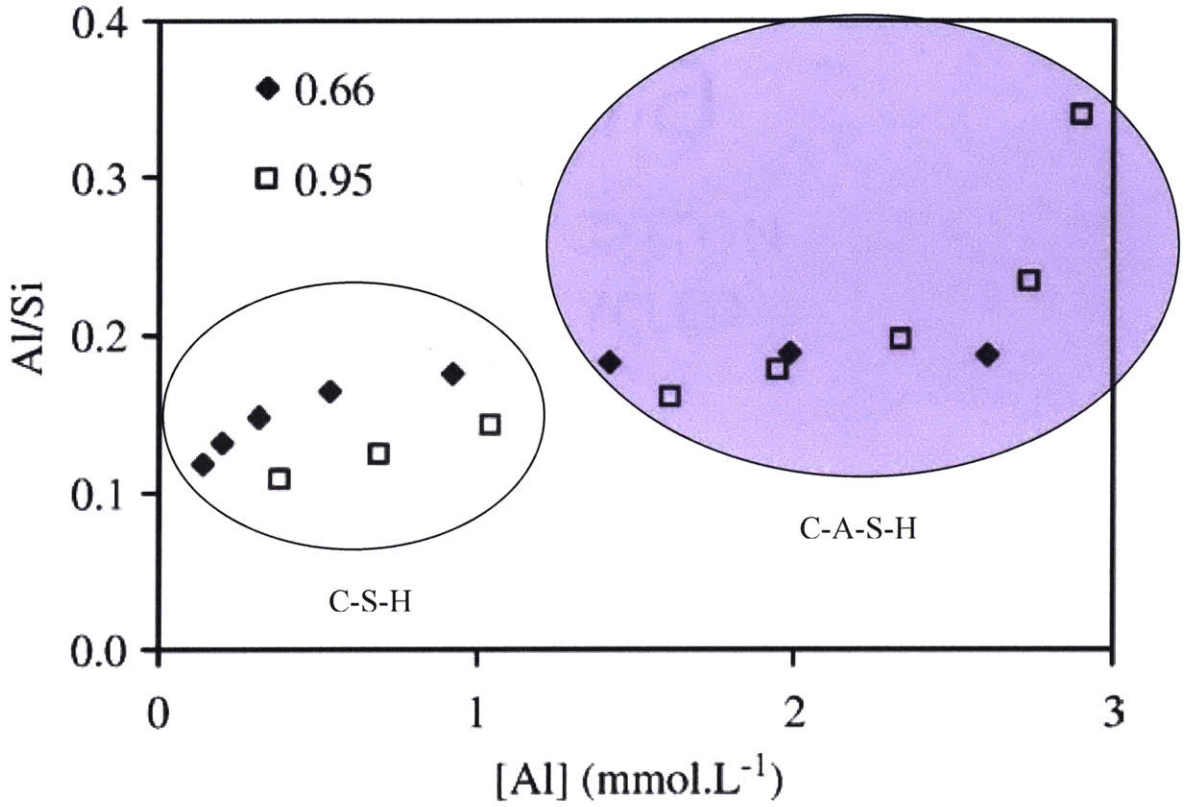

Fig. 8 Al/Si ratio from Pardal *et. al* that was used to determine the C-S-H and C-A-S-H Al/Si ratios [8].

3.4 Synchrotron XRD analysis

The synchrotron x-ray diffraction data was analyzed for phases with High Score Plus, and then plotted in Igor Pro. Figure 9 shows the 5 sodium sulfate samples plotted with respect to arbitrary units to show the relative intensities of the peaks.

Thendardite (denoted by blue squares) transforms into Mirabilite (green circles) due to the accelerated electrokinetic treatment. The applied current led to a temperature increase above 32°C. Mirabilite forms in the higher heat, from the recrystallization of the anhydrous sodium sulfate to its hydrous form.

The presence of Aphthitalite shows that there is insufficient sulfate present in the clinker to maintain the alkalis as their sulfates, and the Na_2O is considered to enter the C_3A where it normally increased the reactivity in the system.

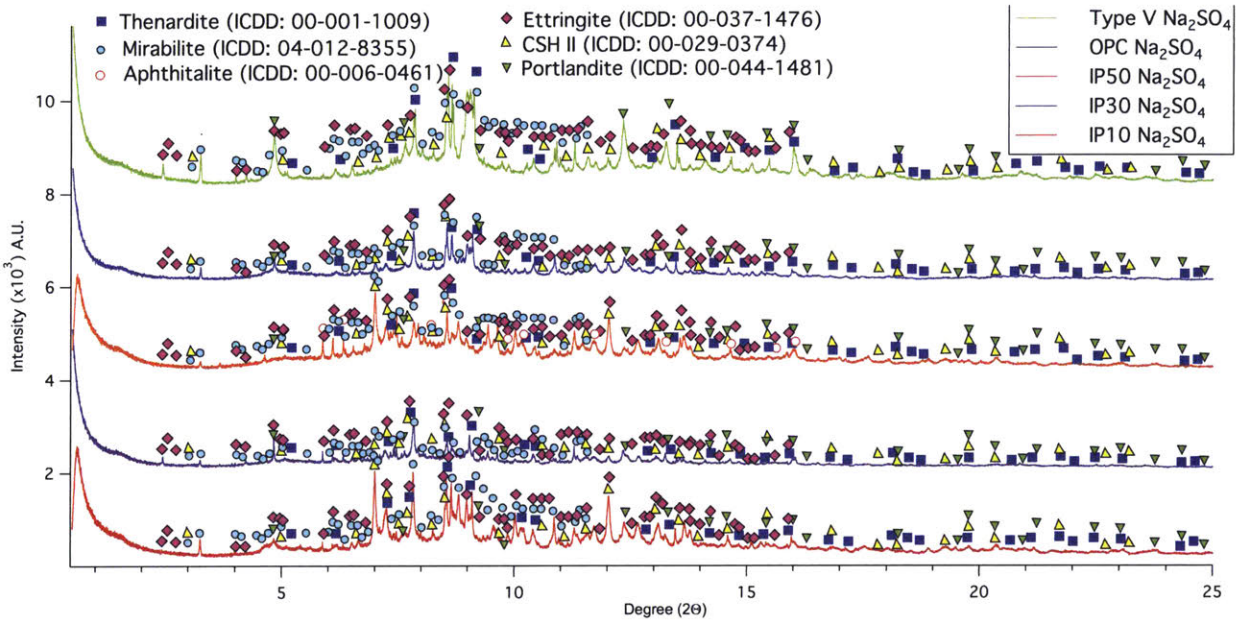

Fig. 9 XRD analysis for sodium sulfate samples

In Figure 10, the x-ray diffraction data shows crystalline peaks for the C-A-S-H gel and M-S-H phases. There are more crystalline M-S-H phases present in the magnesium sulfate sample than the sodium sulfate sample. The crystalline M-S-H leads to an increased porosity in the system, as the shapes of the crystalline M-S-H and C-S-H are not compatible. The increased porosity allows for an easier transport mechanism for sulfate attack, making the samples more susceptible to the strength degradation that comes with sulfate attack.

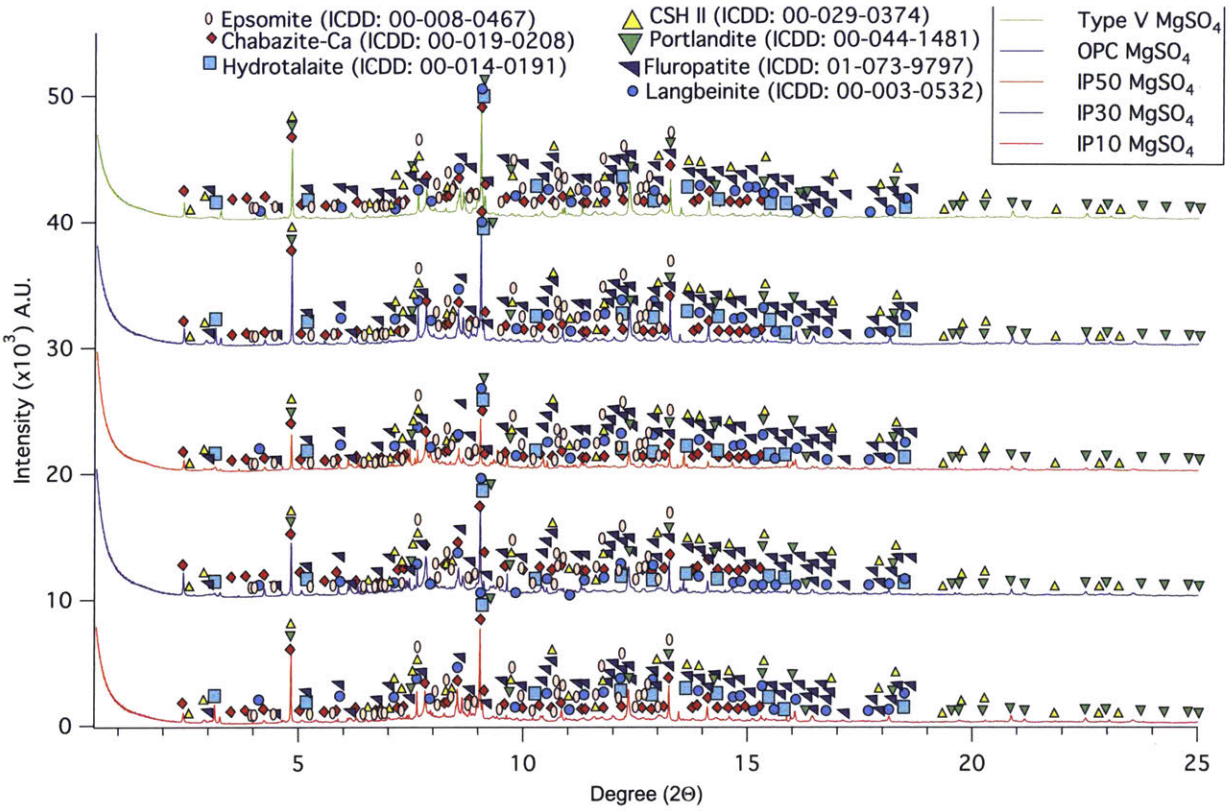

Fig. 10 XRD Analysis for magnesium sulfate samples

3.5 Scanning Electron Microscopy

The SEM images show the structure of the ettringite compared to the structure of the zeolites. The ettringite can be seen in the top row, in the magnesium sulfate images. These have a conical structure, and are on the order of microns. In the sodium sulfate images, the zeolites have a hexagonal columnar structure, which are on the order of millimeters. The magnesium samples illustrate the ettringite that creates more porosity in the sample, whereas the sodium sulfate samples illustrate the zeolite that do not directly lead to increased porosity as they are of a larger length scale (microns vs. nanometers).

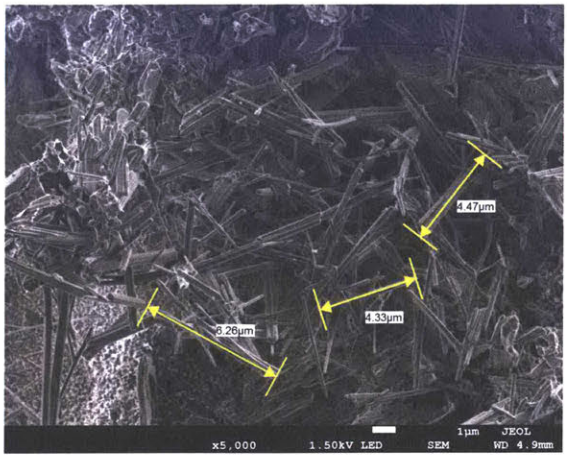

OPC $MgSO_4$ at 5,000X

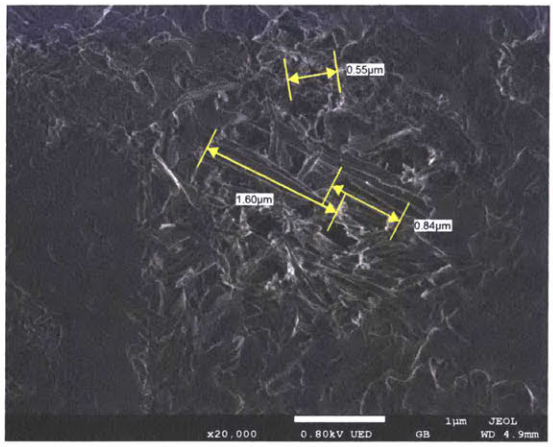

Type V $MgSO_4$ at 20,000X

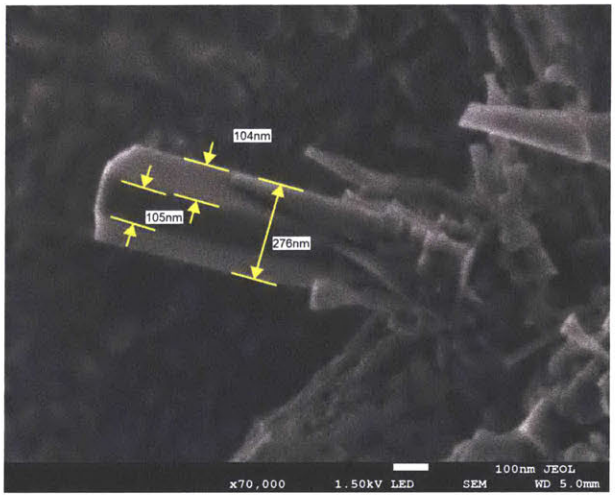

OPC Na_2SO_4 at 70,000X

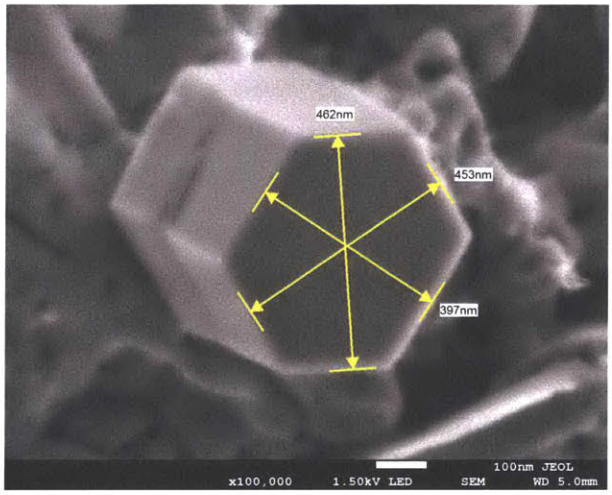

IP30 Na_2SO_4 at 100,000X

Fig. 11 Scanning Electron Microsopy images

3.6 General Discussion

The sodium sulfate attack samples illustrate a higher C-S-H content due to the pozzolanic cement paste which has enhanced the protective action of the silicate gel on the aluminate hydrates. The small sized calcium hydroxide crystals covered and shielded by C-S-H may be responsible for prevention of ettringite formation. The ettringite content is higher in magnesium than sodium, as the natural pozzolana cements are subject to sodium sulfate, the ettringite formation occurs without sufficient expansion, this could be due to ettringite forming in voids. However, the replacement of pozzolana from Portland cement decrease C_3A, but increases the total Al_2O_3 content in the

cement, thus the protective action cannot be explained based on the concentration of calcium sulphoaluminate hydrate.

The magnesium sulfate attack samples show that $Ca(OH)_2$ and gypsum occur inside the cement matrix through redistribution of Ca^{2+} ions between C-S-H. The addition of $MgSO_4$ in the system leads to formation of amorphous M-S-H along with M-A-S-H and brucite. M-S-H phases are weaker in strength compared to C-S-H and the morphology of M-S-H is spherical compared to the columnar C-S-H. Due to the presence of irregular shapes, porosity of the matrix increase, thus affecting the overall strength of the matrix. The formation of M-A-S-H and C-A-S-H phases means that the chemically bound water inside the C-S-H and M-S-H has been affected, as the hydroxide ions diffuse out from the paste and sulfate ions diffuse inwards from the surface.

Overall, it was found that the volcanic ash samples performed better than their OPC and Type V counterparts. However, the IP50 sample specifically did not show much of an advantage in compressive strength or sulfate resistance. This may be due to the incorporation of too much volcanic ash, which leads to a point where the volcanic ash is not participating in the hydration reaction. Rather than incorporating into the cementitious matrix, it is present as volcanic ash precipitates. Therefore, the optimal volcanic ash replacement is between 10-30%. However, more testing is required to get a more exact percentage for optimal replacement.

4. Conclusion and Future Work

Magnesium sulfate attack has a more deleterious effect on the cement paste than sodium sulfate. This may be due to the higher amount of calcium hydroxide and C-S-H that help in enhancing strength and preventing the effects of sulfate attack in sodium sulfate. The spherical M-S-H that is present in the crystalline form in the magnesium sulfate samples creates more pores

than the columnar C-S-H zeolite structure. This makes M-S-H weaker than the C-S-H hydration product.

The strength of the cement paste samples is directly related to the hydration products in the system. C-S-H and C-A-S-H specifically, play an important role in the strength of the cement paste samples.

The optimal replacement of OPC with volcanic ash is 10-30% as these samples offer the best sulfate resistance and compressive strength increase. Future testing is required to determine a more specific range of OPC replacement. This could be done through more iterations of testing, and a use of pore analysis to analyze the reaction of the volcanic ash in the system.

Future work will incorporate water absorption testing, and SEM EDS phase analysis. Ettringite structure should also be analyzed with small angle neutron scattering. Degradation of the sulfate attack occurs over various time scales, so it is important to complete additional testing over a larger time scale that is more representative of the field conditions. The long-term effect of water may lead to additional ettringite formation. The volcanic ash should be engineered to have a uniform particle size, to see if the uniformity will lead to increased sulfate resistance and strength.

References

[1] V. Ching, F.D.K., Jarzombek, M, Prakash, *A Global History of Architecture*. Wiley, 2011.

[2] B. J. Nichelson, "Cement," *Salem Press Encyclopedia of Science*. Salem Press, 2016.

[3] W.-S. Chiang, G. Ferraro, E. Fratini, F. Fidi, Y.-Q. Yeh, U.-S. Jeng, S.-H. Chen, and P. Baglioni, "Multiscale structure of calcium-and magnesium-silicate-hydrate gels," *J. Mater. Chem. A*, no. 32, pp. 12991–12998, 2014.

[4] H. Cardenas, K. Kupwade-Patil, and S. Eklund, "Recovery from Sulfate Attack in Concrete via Electrokinetic Nanoparticle Treatment," *J. Mater. Civ. Eng.*, vol. 23, no. 7, pp. 1103–1112, 2011.

[5] ASTM C1012/C1012M-15, "Standard test method for length change of hydraulic-cement mortars exposed to a sulfate solution," *ASTM Int. West Conshohocken, PA*, vol. 11, pp. 5–9, 2015.

[6] W. C. Oliver and G. M. Pharr, "experiments," *J. Mater. Res.*, vol. 7, no. 6, pp. 1564–1583, 1992.

[7] A. Mendes, W. P. Gates, J. G. Sanjayan, and F. Collins, "NMR, XRD, IR and synchrotron NEXAFS spectroscopic studies of OPC and OPC/slag cement paste hydrates," *Mater. Struct.*, vol. 44, no. 10, pp. 1773–1791, 2011.

[8] X. Pardal, I. Pochard, and A. Nonat, "Experimental study of Si–Al substitution in calcium-silicate-hydrate (C-S-H) prepared under equilibrium conditions," *Cem. Concr. Res.*, vol. 39, no. 8, pp. 637–643, 2009.

[9] G. Constantinides and F. J. Ulm, "The effect of two types of C-S-H on the elasticity of cement-based materials: Results from nanoindentation and micromechanical modeling," *Cem. Concr. Res.*, vol. 34, no. 1, pp. 67–80, 2004.

[10] H. M. Jennings, J. J. Thomas, J. S. Gevrenov, G. Constantinides, and F. J. Ulm, "A multi-technique investigation of the nanoporosity of cement paste," *Cem. Concr. Res.*, vol. 37, no. 3, pp. 329–336, 2007.

[11] F. Puertas, M. Palacios, H. Manzano, J. S. Dolado, A. Rico, and J. Rodríguez, "A model for the C-A-S-H gel formed in alkali-activated slag cements," *J. Eur. Ceram. Soc.*, vol. 31, no. 12, pp. 2043–2056, 2011.

[12] J. E. Oh, Y. Jun, and Y. Jeong, "Characterization of geopolymers from compositionally and physically different Class F fly ashes," *Cem. Concr. Compos.*, vol. 50, pp. 16–26,

2014.

[13] M. D. Andersen, H. J. Jakobsen, and J. Skibsted, "Characterization of white Portland cement hydration and the C-S-H structure in the presence of sodium aluminate by 27Al and 29Si MAS NMR spectroscopy," *Cem. Concr. Res.*, vol. 34, no. 5, pp. 857–868, 2004.

[14] S. A. Bernal, J. L. Provis, B. Walkley, R. San Nicolas, J. D. Gehman, D. G. Brice, A. R. Kilcullen, P. Duxson, and J. S. J. van Deventer, "Gel nanostructure in alkali-activated binders based on slag and fly ash, and effects of accelerated carbonation," *Cem. Concr. Res.*, vol. 53, pp. 127–144, 2013.

[15] K. Kupwade-Patil, A. F. Al-Aibani, M. F. Abdulsalam, C. Mao, A. Bumajdad, S. D. Palkovic, and O. Büyüköztürk, "Microstructure of cement paste with natural pozzolanic volcanic ash and Portland cement at different stages of curing," *Constr. Build. Mater.*, vol. 113, pp. 423–441, 2016.

Appendix

Nanoindentation Maps

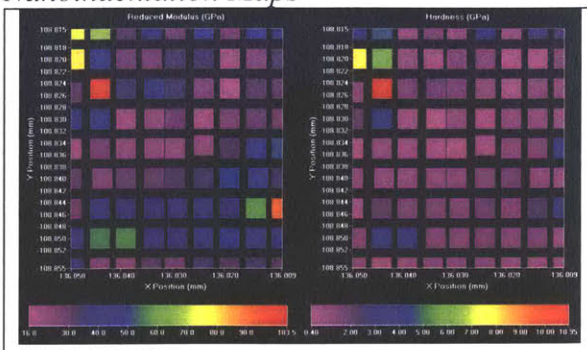

IP10 Na_2SO_4

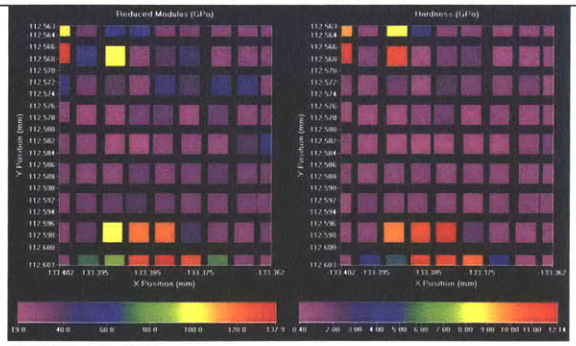

IP10 $MgSO_4$

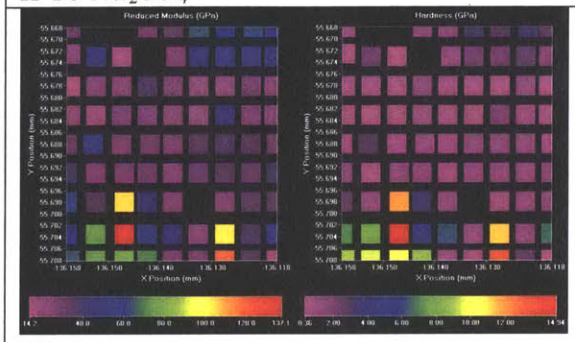

IP30 Na_2SO_4

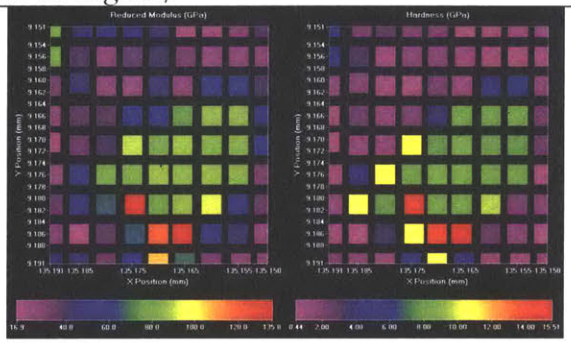

IP30 $MgSO_4$

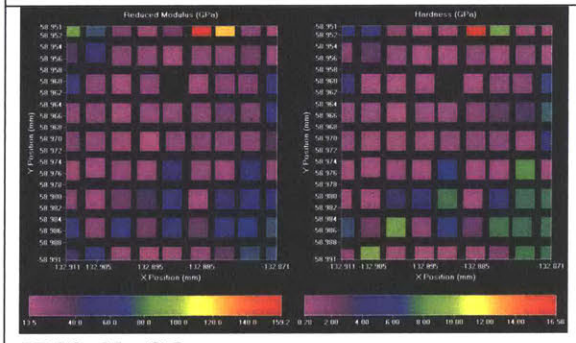

IP50 Na_2SO_4

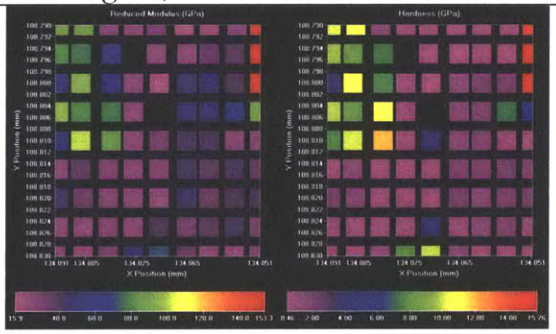

IP50 $MgSO_4$

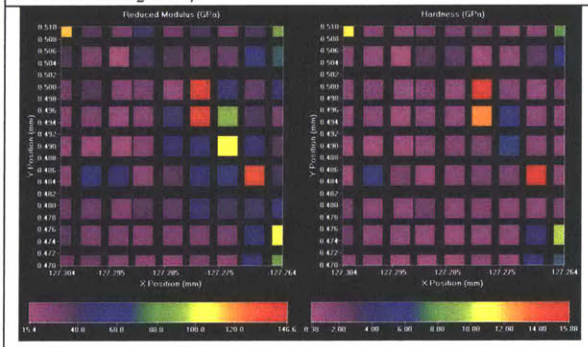

OPC Na_2SO_4

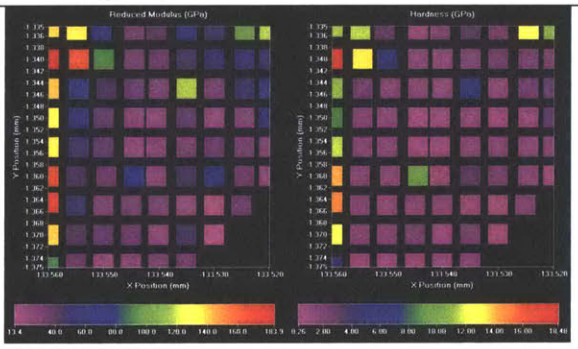

OPC $MgSO_4$

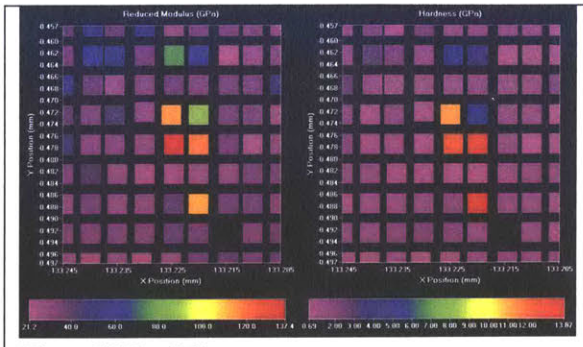

Type V Na_2SO_4

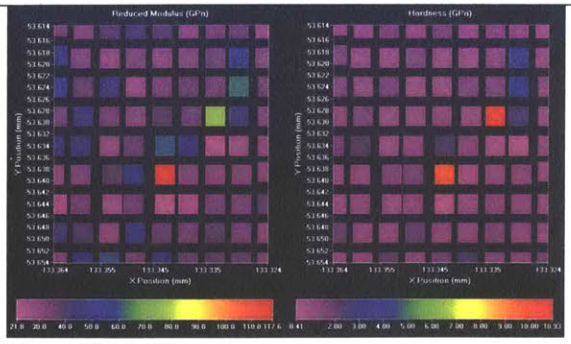

Type V $MgSO_4$